

RESEARCH ARTICLE

10.1002/2015JB012214

Key Points:

- Electrical resistivity and permeability are reduced in the deforming zones at SAFOD
- Deforming zone permeability is low enough to create a barrier to fluid flow across the fault

Correspondence to:

C. Morrow,
cmorrow@usgs.gov

Citation:

Morrow, C., D. A. Lockner, and S. Hickman (2015), Low resistivity and permeability in actively deforming shear zones on the San Andreas Fault at SAFOD, *J. Geophys. Res. Solid Earth*, 120, 8240–8258, doi:10.1002/2015JB012214.

Received 19 MAY 2015

Accepted 8 NOV 2015

Accepted article online 17 NOV 2015

Published online 21 DEC 2015

Low resistivity and permeability in actively deforming shear zones on the San Andreas Fault at SAFOD

C. Morrow¹, D. A. Lockner¹, and S. Hickman¹

¹U.S. Geological Survey, Menlo Park, California, USA

Abstract The San Andreas Fault Observatory at Depth (SAFOD) scientific drill hole near Parkfield, California, crosses the San Andreas Fault at a depth of 2.7 km. Downhole measurements and analysis of core retrieved from Phase 3 drilling reveal two narrow, actively deforming zones of smectite-clay gouge within a roughly 200 m wide fault damage zone of sandstones, siltstones, and mudstones. Here we report electrical resistivity and permeability measurements on core samples from all of these structural units at effective confining pressures up to 120 MPa. Electrical resistivity ($\sim 10 \Omega\text{-m}$) and permeability (10^{-21} to 10^{-22} m^2) in the actively deforming zones were 1 to 2 orders of magnitude lower than the surrounding damage zone material, consistent with broader-scale observations from the downhole resistivity and seismic velocity logs. The higher porosity of the clay gouge, 2 to 8 times greater than that in the damage zone rocks, along with surface conduction were the principal factors contributing to the observed low resistivities. The high percentage of fine-grained clay in the deforming zones also greatly reduced permeability to values low enough to create a barrier to fluid flow across the fault. Together, resistivity and permeability data can be used to assess the hydrogeologic characteristics of the fault, key to understanding fault structure and strength. The low resistivities and strength measurements of the SAFOD core are consistent with observations of low resistivity clays that are often found in the principal slip zones of other active faults making resistivity logs a valuable tool for identifying these zones.

1. Introduction

Electrical resistivity is a useful tool for determining the internal structure and physical properties of fault zones. Resistivity studies are employed on many scales, from magnetotelluric (MT) data [Ritter *et al.*, 2005] to borehole logging and measurements on laboratory samples. These different scales are all important for providing a complete picture of fault structure. MT studies show broad zones of resistivity behavior, whereas borehole studies focus on much narrower regions that cannot be discerned with MT data. Similarly, laboratory measurements on the millimeter to centimeter scale show many lithology variations that are undetectable in borehole data.

Numerous resistivity studies have been conducted on active fault zones around the world (see for instance, Yamaguchi *et al.* [2001] and Pezard *et al.* [2000], Hyogo-ken Nanbu (Kobe) earthquake, Japan; Hung *et al.* [2007] and Yang *et al.* [2002], Chelungpu fault, Chi-Chi earthquake, Taiwan; Yamaguchi *et al.* [2007], western Tottori earthquake, Japan; and Wannamaker *et al.* [2002], Alpine fault, New Zealand). The resistivity structure of various sections of the San Andreas Fault in California, have been modeled by Mazzella [1976], Phillips and Kuckes [1983], Unsworth *et al.* [2000], Unsworth and Bedrosian [2004], and others. These fault zone studies all report low electrical resistivity zones (also called fault zone conductors) due to enhanced fluid conductivity within the associated fracture zones around the fault core. Fault zone conductors are also associated with low-seismic-velocity zones [Zoback *et al.*, 2010; Jeppson and Tobin, 2015]. Combined analysis of these physical properties along with petrographic studies provides a detailed picture of fault structure.

2. The San Andreas Fault Observatory at Depth

This paper focuses on the San Andreas Fault, a right-lateral strike-slip fault composed of a number of segments that exhibit either locked or creeping behavior. The San Andreas Fault Observatory at Depth (SAFOD) drill site is located in a transition zone between a creeping segment of the San Andreas Fault to the north and a locked segment to the south. Numerous microearthquakes occur along the active trace(s)

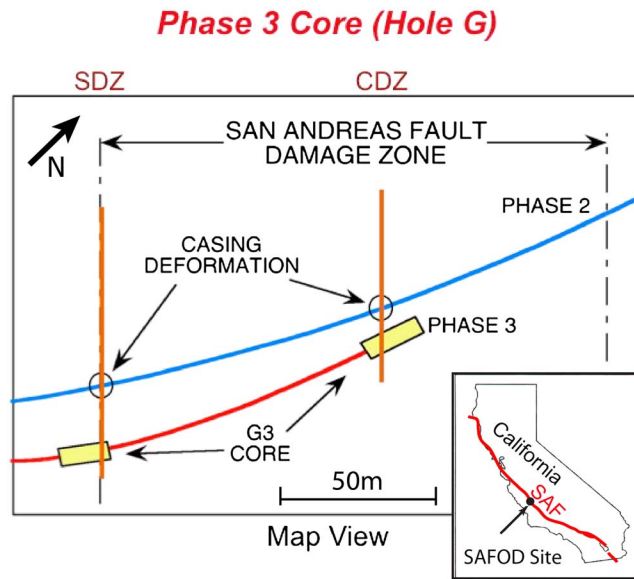


Figure 1. Map view of SAFOD Phase 2 and Phase 3 drill holes with an inset of the State of California showing the SAFOD drill site along the San Andreas Fault (SAF).

of the fault. The SAFOD borehole (35.974028°N, 120.552425°W) is 1.8 km SW of the fault near Parkfield, California. It was initially drilled vertically to a depth of around 1.5 km and then deviated in a direction toward the microearthquakes on the fault, crossing the fault at a depth of approximately 2.7 km during three separate phases of drilling [Zoback et al., 2010]. A map view of boreholes from Phase 2 (blue) and Phase 3 Hole G (red) is shown in Figure 1 along with an inset of the State of California showing the SAFOD drill site location along the San Andreas Fault.

tion, indicating areas of active creep, is highlighted along the Phase 2 hole, defining the southwest deforming zone (SDZ) and the central deforming zone (CDZ) [Zoback et al., 2010, 2011]. These two features were the targets of Phase 3 drilling, where core material was retrieved from approximately 2.7 km depth. Phase 3 Hole G was drilled subparallel to the Phase 2 hole and as indicated in Figure 1, core was retrieved from within 30 m of the locations where casing deformation was observed in the Phase 2 hole.

The seismic velocity and electrical resistivity log (deep depth of investigation (DOI), see below for explanation) from 3100 to 3500 m measured depth (MD) in the Phase 2 hole is shown in Figure 2 [Zoback et al., 2010].

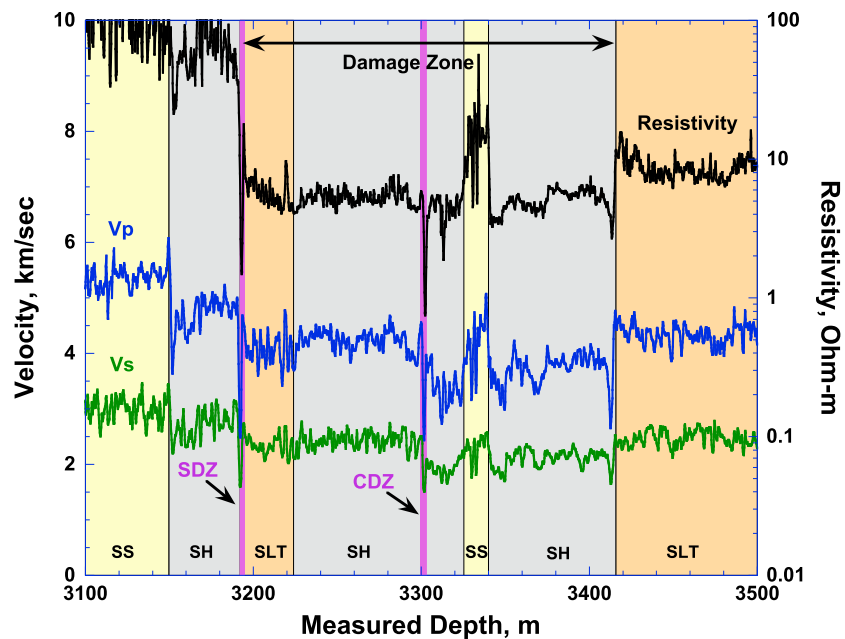


Figure 2. Seismic velocity and electrical resistivity log from Phase 2 borehole, showing the damage zone (horizontal arrow) and the SDZ and CDZ. Lithology is indicated at the bottom: SS = sandstone; Sh = shale; SLT = siltstone. Measured depth refers to the Phase 2 hole.

MD refers to measured depth in the borehole (see Appendix A). Also shown in Figure 2 are the generalized geologic units (see *Bradbury et al.* [2011] for a complete description of lithology). The damage zone, indicated by the horizontal arrow, can be clearly identified as a broad area of reduced velocity and resistivity that closely follows the lithology and is interpreted to be a result of both physical damage and chemical alteration associated with faulting. The downhole log shows details that would not be detected with MT. For instance, although MT would catch the 1 order of magnitude resistivity drop at the SW boundary of the damage zone (3200 m), the smaller increase at 3420 where the damage zone transitions back into country rock would be largely undetectable. Hence, an MT survey would indicate a single contact at ~3200 m.

The details present in the downhole log show that even within the damage zone, lithology-related variations occur, such as the increased velocity and resistivity in the sandstone unit (3322–3340 m) compared to the surrounding shales. The CDZ and SDZ appear as narrow bands, approximately 1.6 and 2.6 m wide, respectively, within the damage zone and are composed of foliated fault gouge with 60–65% phyllosilicate material. The SDZ is adjacent to the sandstone country rock that marks the SW boundary of the damage zone, whereas the CDZ is located near the middle of the damage zone. The sharply lower resistivity and velocity within these two deforming zones compared to the rest of the damage zone is difficult to distinguish on the scale of Figure 2. Enlarged views in the vicinity of the SDZ and CDZ are shown in Figure 3, where a distinctive drop in both resistivity and velocity is observed. In these plots, the width of the deforming zones (gray shading), determined by petrographic analysis of Phase 3 core, has been superimposed on the Phase 2 logs with depth registration determined by natural gamma data. When aligned this way, velocity lows correspond exactly with the CDZ and SDZ intervals. A detailed description of depth correlations between Phase 2 and Phase 3 structures is given in *Zoback et al.* [2010], supporting information, part of which is reproduced in Appendix A below. Note that the resistivity low in Figure 3 is offset from the velocity low by about 1 m. This shift occurs over much of the log and appears to be a systematic problem with the recorded depth of the resistivity data.

Resistivity is shown with shallow (10"/0.25 m), medium (30"/0.76 m), and deep (120"/3.05 m) depth of investigation (DOI) values. DOI refers to the distance into the formation for which resistivity is determined. It is accomplished by processing the multichannel resistivity data using different weighting algorithms and is useful for determining the depth of penetration of the conductive drilling mud. In the examples shown in Figure 3, the 10" DOI resistivity is consistently low, suggesting penetration of the drilling mud to at least 0.25 m. A deeper DOI minimizes the contribution of drilling mud invasion on the estimate of formation resistivity. Note that the spread in the resistivity values is less in the deforming zones due to the reduced mud invasion into the low permeability gouge material as well as the smaller contrast in resistivity between mud and foliated gouge. Phase 3 drilling mud had a high brine content to help stabilize the clay-rich core samples that were retrieved, making it more conductive than the Phase 2 mud. Using this high-conductivity mud had a significant effect on the Phase 3 resistivity log. For this reason, we compare the Phase 3 core resistivity values with Phase 2 resistivity log data.

We have conducted combined electrical resistivity and permeability measurements on selected intact core specimens from Phase 3 Hole G of the SAFOD borehole (depicted in Figure 1). All samples were oriented parallel to the borehole axis. Permeability results were reported previously in *Morrow et al.* [2014]. We now present the resistivity measurements, showing how resistivity of core samples is related to both the co-measured core permeability data and the Phase 2 wireline log resistivity. Detailed sample descriptions of the materials used in this study can be found in *Morrow et al.* [2014], Appendix 1.

3. Experimental Procedure

3.1. Solid Core Samples

Solid samples of selected SAFOD core rocks from Phase 3 Hole G were fashioned into wafers 1.9 × 1.9 cm square and between 0.4 and 0.9 cm long, depending on material availability. In some samples, corners or edges were missing due to irregularities in the original core material. When this occurred, epoxy was added to fill out the deficient space (but not included in the cross-sectional area calculations). The surfaces of the samples were then hand lapped to a smooth finish on a fine diamond wheel. Electrical resistivity and permeability were determined simultaneously for samples saturated with a brine solution designed to be equivalent to formation fluid in the SAFOD drill hole. The solution constituents, in grams per liter, were: Cl⁻, 13.32; Na⁺, 5.34; Ca²⁺, 2.77; and K⁺, 0.22. The measured fluid conductivity was 3.4 S/m at 22.7°C.

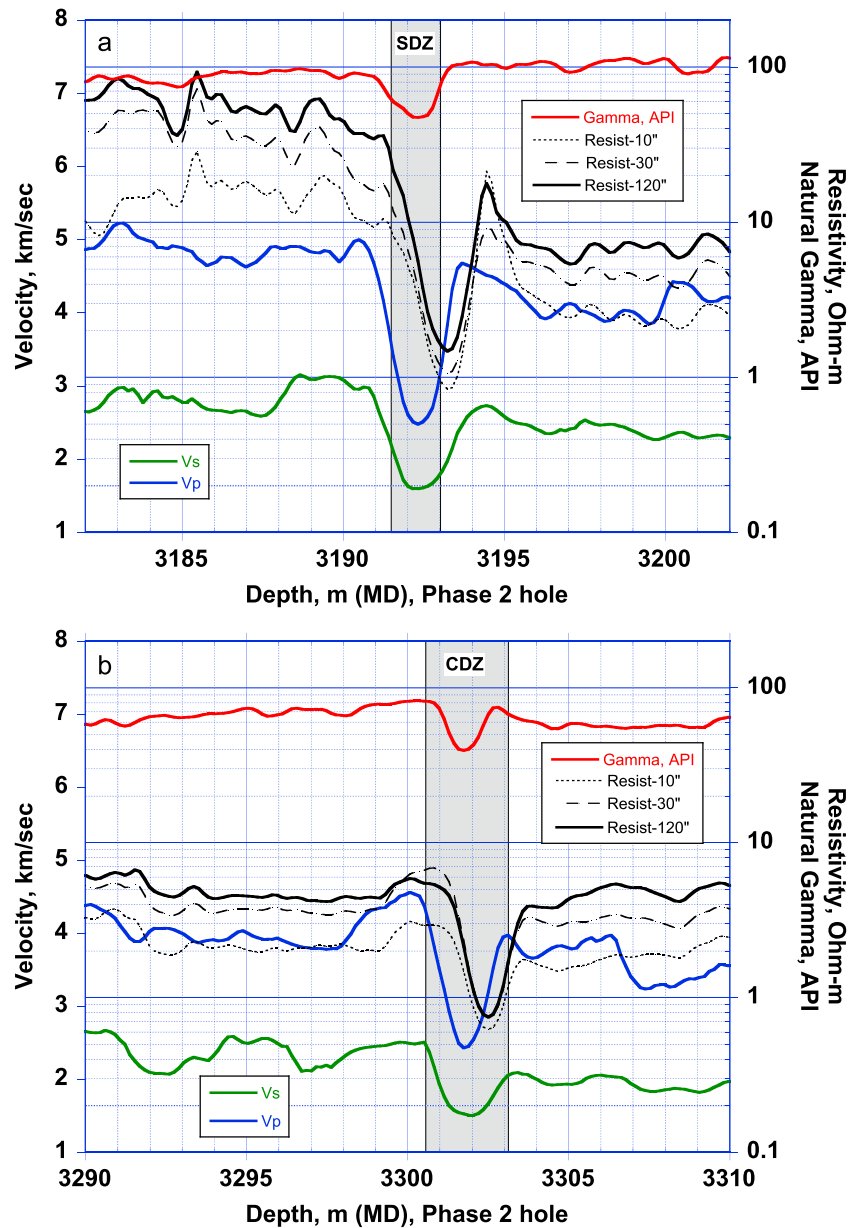


Figure 3. Expanded portions of Figure 2. (a) SDZ region including natural gamma and shallow (10"), medium (30"), and deep (120") depth of investigation (DOI) values for resistivity. (b) Similar plot for CDZ region. Depths are for the Phase 2 borehole. Velocity and resistivity lows correspond to the deforming zones. Raw resistivity data appear to be offset by 1 m.

Berea sandstone wafers, (1.9 cm square faces and 0.65 cm thick), were placed on the ends of the prepared SAFOD samples to assure uniform flow of fluid into and out of the rock specimens. Berea sandstone has a permeability many orders of magnitude higher than the SAFOD samples and does not interfere with the permeability measurements. Sample resistivities were corrected for the Berea wafers as described below. This rock sandwich was placed in a polyurethane jacket to isolate the sample from the silicone oil confining fluid and then secured to steel end plugs that contained a pore fluid inlet and outlet. A schematic of the experimental system is shown in Figure 4.

Electrical resistivity and permeability were measured at effective confining pressures, P_{eff} of 10, 20, 40, 70, 100, and 120 MPa in a pressure vessel at $23.0 \pm 0.5^\circ\text{C}$. $P_{eff} = P_c - P_p$ where P_c and P_p are the confining and pore pressures, respectively. In each run, the sample column was placed in the pressure vessel and evacuated. Then a small confining pressure was applied, and brine was introduced into the sample. Confining and pore pressures were

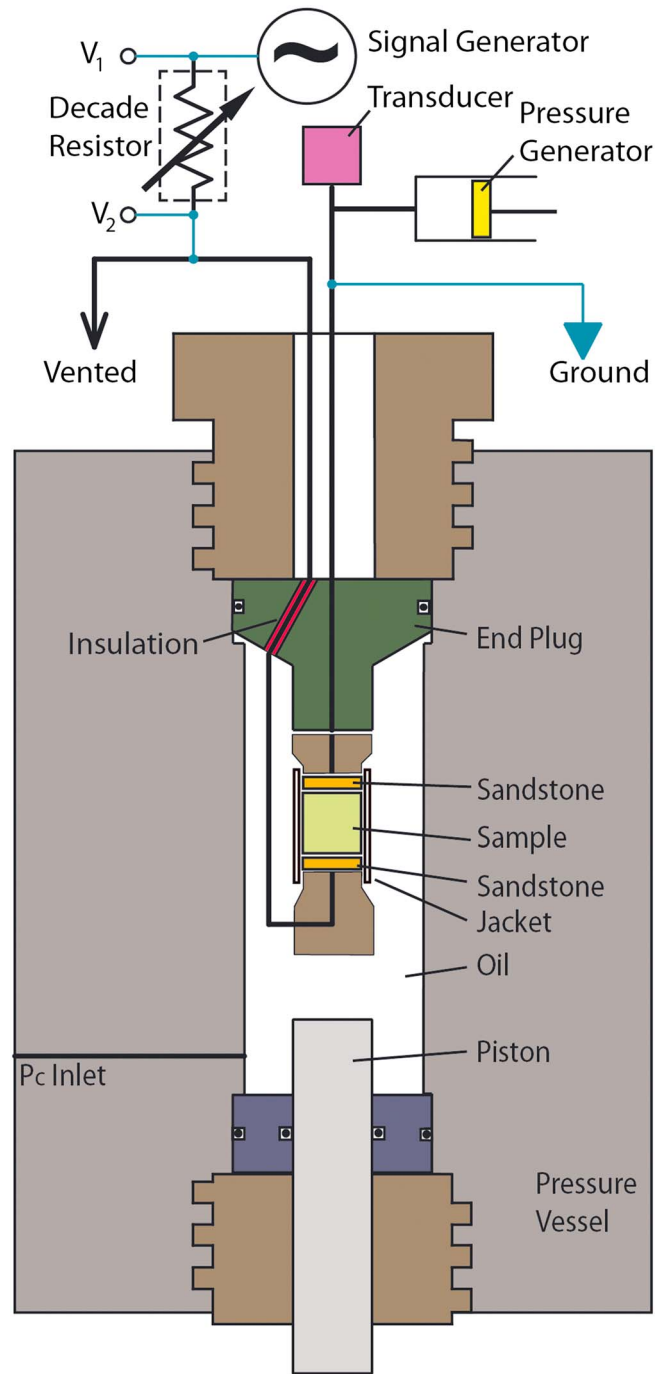


Figure 4. Schematic diagram of the experimental apparatus.

then increased to the initial run conditions ($P_c = 10.50$ MPa gauge pressure, $P_{p_high} = 1.00$ MPa gauge pressure and $P_{p_low} =$ atmospheric pressure). Introducing the brine at very low effective pressure helps accelerate the time for saturation and establishment of steady state flow at the initial run condition to around a few hours. After each effective pressure step, steady state flow was established for periods of hours to days, as needed, by maintaining the inlet pore pressure of the sample at 1.00 ± 0.01 MPa using a computer-controlled pressure generator and venting the low pressure side to the atmosphere. The low side pore pressure tubing was brine filled to assure that no air entered the sample once the measurement sequence began. This tubing was also electrically insulated from the pressure vessel so that electric current in the resistivity measurements flowed through the sample.

Electrical resistance of the samples was measured at each effective pressure step using a two-electrode system. Excitation was provided by a 200 Hz sine wave generator (to minimize electrode polarization) with nominal peak to peak voltage of 3 V. A precision decade resistance box was connected in series with the sample assembly and was adjusted until the voltage drop across the sample column matched the voltage drop across the box. Under this condition, resistance of the sample + sandstone wafers is the same as the resistance of the decade box and can be read directly from the box. Resistivity of brine-saturated Berea sandstone was measured separately and used to compute the resistance of the Berea sandstone wafers placed on the ends of the sample. Wafer resistance increased with P_{eff} from 65 to 104 Ω . This resistance was subtracted from the total sample + sandstone resistance to give sample resistance, R . Finally, resistivity of the SAFOD samples, ρ , was calculated according to

$$\rho = \sigma^{-1} = RA/L, \quad (1)$$

where A and L are the cross-sectional area and length of the sample, respectively, and σ is the sample conductivity. Combined sources of error in determining resistivity from equation (1) are typically less than 1%. For particular samples, especially the foliated gouge, sample preparation was difficult and uncertainties in A/L , and therefore ρ , are estimated at $\pm 5\%$.

Fluid-saturated rocks, especially fault zone material that contains clay, can have multiple conduction mechanisms related to ionic diffusion and chemical reactions. As a result, resistivity is frequency dependent and contains phase differences between electrical potential and resulting current flow. *Olhoeft* [1980] has discussed the desirability of measuring frequency-dependent complex resistivity of water saturated rocks using a four-electrode system. When properly constructed, this will minimize the effects of electrode polarization and unwanted capacitive and inductive coupling in the measuring system. Testing samples at high pressure with a four-electrode system is technically challenging [*Lockner and Byerlee*, 1985, 1986] and is beyond the scope of the present study, especially since we have carried out combined high-pressure permeability/resistivity measurements. The most important compromises that we have made by using a two-electrode system are (1) resistivity is determined at a single frequency, (2) the measurements lack phase information that would provide permittivity, and (3) an unknown contribution of electrode polarization to the measured resistivity. In terms of comparison to borehole log data, electrode polarization is probably the most serious problem. We have attempted to minimize this source of error by using a 200 Hz measurement frequency. It should be noted that borehole resistivity measurements were obtained differently [*Zoback et al.*, 2011]. Logging was carried out by a private contractor using a Baker Hughes induction array (High-Definition Induction Log). With this logging tool, data from six subarrays were collected at eight frequencies (10–150 kHz) and processed to correct for skin effect. The reported values (Figures 2 and 3) have been projected to zero (DC) frequency. Thus, our core measurements, at 200 Hz, should be the same or slightly higher than the corresponding borehole measurements.

A direct comparison of laboratory sample resistivity to wireline log resistivity depends on the brine used in the laboratory tests. Obtaining in situ pore fluid from the SAFOD borehole proved to be difficult, and no reliable fluid samples were collected from the damage zone. The fluid that was replicated in our tests came from deeper in the borehole (NE of the San Andreas Fault) within the Great Valley Formation. When fluid samples eventually become available from the damage zone, our results can be appropriately adjusted. This would amount to adjusting all results by a common factor. Thus, relative variations in resistivity between samples should reflect the relative changes in the in situ rock resistivity. Another potential source of error occurs in the lowest permeability samples that include the foliated gouge. In this case, permeability was so low that it was not feasible to flush samples with brine to assure that we had exchanged residual pore fluid with the test brine. Since we attempted to use brine that was similar in composition to the in situ pore fluid, this should represent a small, but nevertheless unknown, source of error. Test brine contained mainly NaCl [see *Morrow et al.*, 2014] and had conductivity of $\sigma_w = 3.4 \text{ S/m}$ at 22.7°C, resulting in fluid resistivity of $\rho_w = 0.29 \Omega\text{-m}$.

In the steady flow tests, flow rate of pore fluid through the samples was determined by measuring the change in volume of the pore pressure generator with time. Permeability was then calculated at each effective pressure according to Darcy's law:

$$Q/A = k/\mu(\Delta P/\Delta x), \quad (2)$$

where Q is the volumetric flow rate, A is the cross-sectional area of the sample, k is permeability, μ is the dynamic viscosity of water at the temperature and pressure of the experiment (0.95 centipoise for these conditions),

and $\Delta P/\Delta x$ is the pore fluid pressure gradient across the length of the sample. For samples that could not be prepared with precisely square cross sections, actual cross-sectional area was determined and used in both the resistivity and permeability calculations. Accuracy of the permeability determinations was approximately $\pm 5\%$ for values above 10^{-20} m^2 and $\pm 10\%$ for values below 10^{-20} m^2 .

Selected intact samples of foliated gouge were deformed to 10% axial strain after the permeability and resistivity were measured as a function of increasing effective pressure. For these samples, the final effective pressure of the series (typically 70 or 100 MPa) was held constant, while axial shortening was imposed at a rate of $1 \mu\text{m/s}$ (a nominal strain rate of about 10^{-4} s^{-1}). After every 0.5 mm of axial shortening, the piston was held fixed for several hours while permeability and resistivity were measured. In these experiments, differential stress (= axial stress – confining pressure) is recorded as a function of axial shortening. Because these weak, highly plastic samples deformed by barreling rather than forming discrete shear planes, we report strength in terms of differential stress rather than coefficient of friction. In these tests, permeability and resistivity were computed based on the changing length to area ratio of the sample.

3.2. Sheared Gouges

Because the deforming zones contain a high percentage of weak minerals that directly affect the behavior of the San Andreas Fault [e.g., Lockner *et al.*, 2011], it is of interest to determine the coefficient of friction of the foliated gouge in conjunction with the resistivity and permeability experiments. To this end, cross-fault resistivity and permeability of crushed gouge material during frictional shearing were measured for samples from both the southwest and central deforming zones using procedures similar to those described above. The gently crushed and sieved gouges (<0.15 mm diameter grains) were mixed with brine to form a paste. This was applied in a 2 mm layer on the saw cut surface of Berea sandstone cylinders that were cut at an angle of 30° to the sample axis. Frictional shearing experiments were conducted at a constant effective normal stress on the simulated fault of 120 MPa, similar to the estimated normal stress resolved on the SAF at the recovered depth. Pore pressure was fixed at 1 MPa at the inlet of the sample, and vented to atmospheric pressure at the outlet, so that brine flowed through the sample continuously. First, electrical resistivity and permeability were measured over a period of several hours before any shearing took place. Then sliding was initiated at an axial shortening rate of $0.2 \mu\text{m/s}$ for 3 mm of axial displacement. The piston was fixed for a period of 4 to 14 h, during which permeability and resistivity were measured again with the sample in a stationary state. Sliding continued in a similar manner with pauses at 6 mm and 9 mm axial displacement for additional permeability and resistivity measurements. The measured permeability and resistivity were corrected for the changing cross-sectional area of the sample during sliding and the decrease in thickness of the gouge layer with applied pressure.

4. Results

4.1. Intact Samples at Hydrostatic Pressure

Measured resistivity, ρ , of foliated gouge and damage zone rocks spans 3 orders of magnitude, ranging from around 3 to 3000 $\Omega\text{-m}$, partly reflecting the varying porosity and clay content of the cores (Figures 5a and 5b and Table 1). Note that the foliated gouges had the lowest values. Other samples were sandstones, shales, and siltstones (Figure 2). Resistivity increased as a function of effective pressure, following a consistent trend due to the closure of cracks and pores. Corresponding permeabilities of the same samples as a function of effective pressure are shown in Figures 5c and 5d, spanning more than 7 orders of magnitude, from around $6 \times 10^{-23} \text{ m}^2$ to $2 \times 10^{-16} \text{ m}^2$. Permeability decreased with pressure as expected, and the foliated gouge samples had the lowest values. See Morrow *et al.* [2014] for a more detailed description of the permeability results. Combining data in Figure 5 shows that permeability is inversely related to resistivity (Figure 6), obeying, to first order, a power law relation

$$k = a_0 \rho^{-n} \quad (3)$$

Average slopes range from $n = 2.4$ for a highly permeable siltstone at 3198.84 m to 16 for fine-grained cataclasite to ultracataclasite samples at 3194.76 m and 3196.07 m (Figure 6a). The wide range in exponents reflects the complex dependence of permeability and resistivity on pore shape, tortuosity, and clay content, highlighting the difficulty in relating permeability to resistivity.

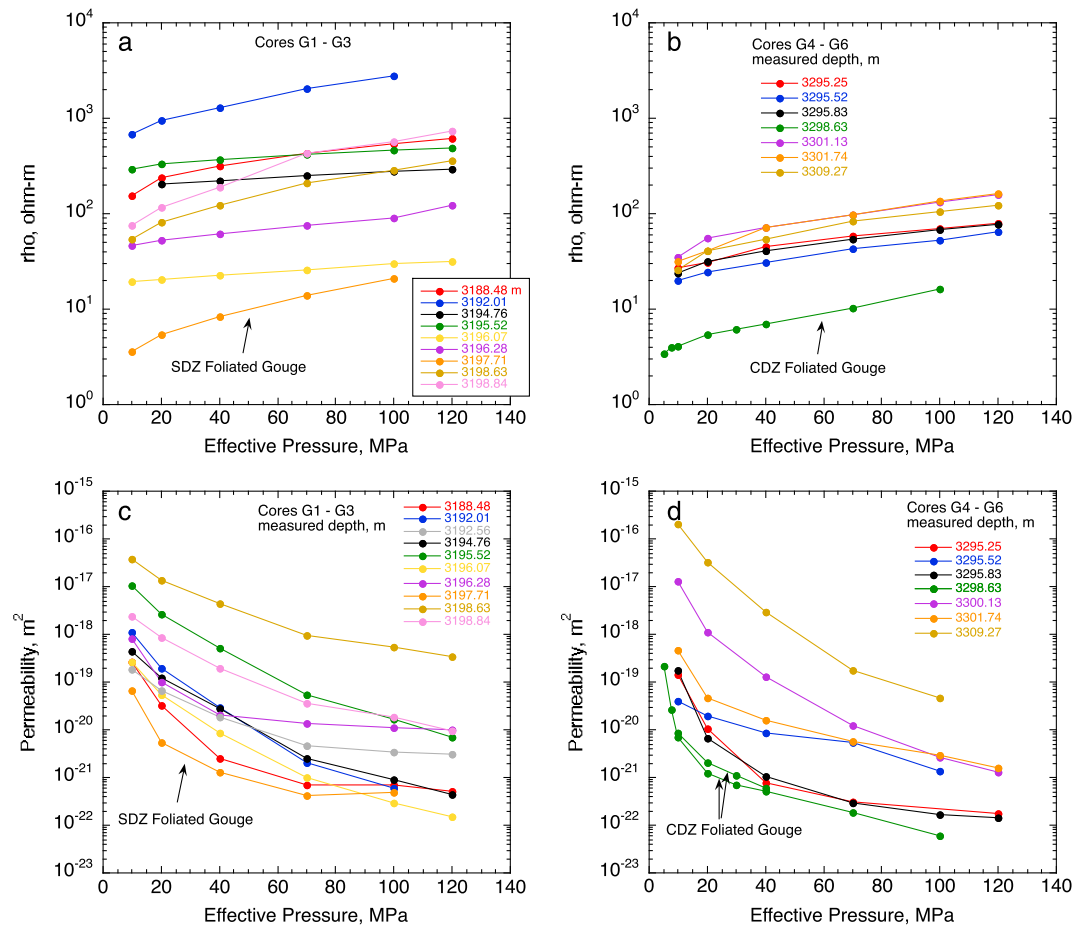


Figure 5. (a) Electrical resistivity as a function of effective confining pressure, P_{eff} , for foliated gouge and damage zone rocks from cores G1–G3. (b) Resistivity for samples from cores G4–G6. (c) Permeability as a function of effective confining pressure, P_{eff} , for the same samples as in Figure 5a. (d) Permeability for the same samples as in Figure 5b. Depths correspond to the Phase 3 borehole measured depths.

Common crustal rocks are typically composed of minerals with high electrical resistivity. Consequently, electrical current flows primarily by ionic transport through the pore fluid. Clays that allow migration of surface charge add an additional conduction mechanism that can contribute to our shale, siltstone, and especially foliated gouge samples. Since most charge transport in wet rock occurs in the pore space, resistivity of brine-saturated rock is strongly dependent on porosity. We determined porosity as a function of pressure for a limited number of sandstone country rock and damage zone shale and siltstone samples by measuring the initial porosity using a submersion method (Table 1), together with the volume of fluid expelled with each increase in effective pressure. Initial porosity of the foliated gouge samples could not be determined by a submersion method due to their friable nature. For these samples, initial porosity was calculated based on the measured total sample density and the density and abundance of the constituent minerals. This is a less accurate method of determining porosity than sample immersion and is reflected by the larger uncertainty in Table 1.

The unconfined porosity (Table 1) as well as pore fluid expelled during pressurization for five samples allows us to estimate residual porosity at an effective pressure of 10 MPa. A comparison of sample conductivity and porosity at 10 MPa is plotted in Figure 7. The foliated gouge is found to be the most conductive of the samples tested. In section 5.1, we interpret the variations in conductivity and especially the relative contributions of surface conduction and electrolyte conduction.

4.2. Deformed and Sheared Samples

While measurements made under hydrostatic conditions reveal a great deal about the behavior of these SAFOD core samples, we know that the foliated gouge in particular is actively deforming and the development of

Table 1. Physical Properties of SAFOD Core Samples

Depth (m)	Rock ^a Type	Density ^b (gm/cc)	Porosity ^b Unconfined	Porosity ^c (10 MPa)	ρ (100 MPa) (Ω -m, 23°C)	ρ (100 MPa) ^d (Ω -m, 113°C)	k (100 MPa) (m^2)
3188.48	SH	2.42	5.0 ± 1.7	4.8 ± 1.8	538.8	140.3	6.92 e ⁻²²
3192.01	SH	2.49	1.9 ± 1.5		2780.0	723.9	5.99 e ⁻²²
3192.56	SH	2.55	2.4 ± 2.5		-	-	3.41 e ⁻²¹
3194.76	SH	2.25	4.4 ± 1.0		275.6	71.8	9.29 e ⁻²²
3195.52	SH	2.66	-		461.1	120.1	1.70 e ⁻²⁰
3196.07	SH	2.11	-		29.8	7.7	2.98 e ⁻²²
3196.28	SH	2.35	5.7 ± 1.0	5.6 ± 1.1	89.4	23.3	1.10 e ⁻²⁰
3197.71	G	-	-		21.0	5.5	4.83 e ⁻²²
3198.63	SLT	2.67	3.9 ± 0.8		288.4	75.1	5.41 e ⁻¹⁹
3198.84	SLT	2.51	4.8 ± 0.8		577.4	150.4	1.81 e ⁻²⁰
3295.25	SH	2.32	8.7 ± 1.1		70.4	18.3	2.15 e ⁻²²
3295.52	SH	2.52	4.6 ± 1.1	4.3 ± 1.2	52.2	13.6	1.36 e ⁻²¹
3295.83	SH	2.40	7.1 ± 0.6		68.2	17.7	1.65 e ⁻²²
3298.63	G	2.03	15.4 ± 3.0	12.4 ± 3.6	16.3	4.2	6.17 e ⁻²³
3300.13	SH	2.34	-		132.0	34.3	2.71 e ⁻²¹
3301.74	SH	2.46	4.9 ± 0.7		134.7	35.1	2.89 e ⁻²¹
3309.27	SH	2.34	7.0 ± 1.2		105.1	27.4	4.65 e ⁻²⁰

^aSH = shale, SLT = siltstone, and G = gouge.

^bSome values could not be measured due to the friable nature of the core material. Porosity of the 3298.63 sample was based on the density of the constituent minerals.

^cPorosity values (%) at 10 MPa used in Figure 7.

^dResistivity values corrected for the temperature at depth.

deformation microstructures can affect physical properties. The frictional strength characteristics of the SAFOD samples have been discussed in *Lockner et al.* [2011] and *Carpenter et al.* [2012], and permeability values during frictional shearing have also been reported in *Morrow et al.* [2014]. Few studies have combined these properties of fault zone materials with electrical resistivity. To this end, resistivity and permeability were determined simultaneously for a representative foliated gouge from 3298.63 m (CDZ) deformed to 10% axial strain at an effective pressure of 70 MPa (Figure 8). Drops in differential stress at 0.5, 1.0, and 1.7 mm of displacement result from sample relaxation when the piston was held fixed during permeability/resistivity measurements. These slow stress drops, resulting from time-dependent creep, are not to be confused with dynamic fracture growth in brittle samples. Resistivity and permeability continued to evolve during deformation as the sample strain hardened and pore structure evolved. Differential stress (and hence sample compaction) did not peak (26.5 MPa) until about 1.3 mm shortening. Resistivity increased from 11 to 22 Ω -m, while permeability dropped an order of magnitude from $5 \times 10^{-21} m^2$ to $5 \times 10^{-22} m^2$ as the sample shortened by 10%. This inverse relationship is similar to the trends observed in Figure 6 for permeability and resistivity under increasing effective pressure.

Intact samples, such as the ones used here, can only be deformed between 10 and 20% axial shortening. Higher strains are achieved using thin layers, usually of disaggregated material, sheared between driving blocks. The permeability and electrical resistivity (normalized relative to the starting value) of a 2 mm layer of disaggregated gouge from the CDZ (3296.86 m), sheared between 30° saw cut pieces of Berea sandstone is shown in Figure 9. The effective normal stress on the simulated fault was held constant at 120 MPa and deformation continued to a nominal shear strain of 4.5. Several other saw cut shearing experiments on samples from other depths (not shown) behaved in a similar manner. That is, neither permeability nor resistivity was much affected by shearing once the sample reached a fully developed plastic flow condition. This is consistent with permeability results during shearing reported in *Morrow et al.* [2014] for a number of different CDZ and SDZ samples where permeability remained fairly constant.

In this experimental configuration, the Berea sandstone driving blocks had a dominant contribution to the resistivity of the sample assembly, making it difficult to accurately extract the resistivity of the gouge layer. This is why we plot relative changes in total sample resistance in Figure 9. These 2 mm gouge layers are initially prepared by smearing the gouge paste on the face of the driving block during sample preparation. This procedure will partially align the clay particles parallel to the sliding surface so that little reorientation is required once shearing commences. In *Morrow et al.* [2014], it was confirmed that shearing experiments on disaggregated samples

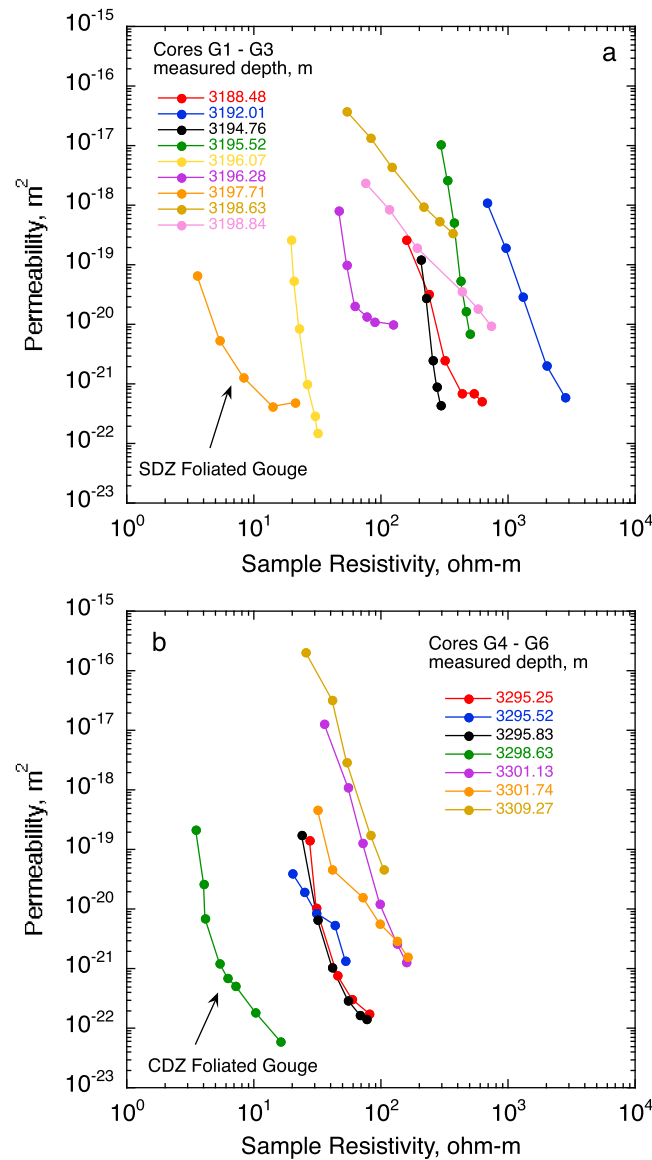


Figure 6. (a) Permeability as a function of electrical resistivity for core samples from cores G1–G3, spanning an effective pressure range from 10 to 120 MPa. (b) Similar plot for samples from cores G4–G6. Measured depths from the Phase 3 hole.

Archie’s law [Archie, 1942] was proposed as an empirical relation between conductivity and porosity for clean sands and sandstones:

$$\frac{\sigma}{\sigma_w} = \frac{1}{a} \phi^m \tag{4}$$

where a and m are empirical constants and as initially proposed by Archie, $a = 1$. Commonly referred to as the cementation factor, m is a geometric parameter that accounts for pore structure. Randomly packed spherical particles give $m \sim 1.2$ and uncemented sands give $m \sim 1.5$. Larger m values indicate a more angular, platy, or otherwise complex nature of the mineral grains, and hence a pore network with higher tortuosity. Log-log plots of field data that contained clays were found to obtain a better fit with a nonzero intercept, and therefore, variable a , although there is no theoretical justification for this [Bussian, 1983]. Timur et al. [1972], for example, compiled data on 1832 sandstone samples and found best fits of $a = 1.13$ and $m = 1.73$. Figure 7 shows variability in the SAFOD data, but when lumped together, the fit to equation (4) (with $a = 1$) yields a slope of $m = 1.60$.

provided a good proxy for intact sample permeability measurements. While we are not able to calculate the exact resistivity of the gouge layer in the saw cut geometry, we do know that it remains relatively constant with shearing. Further tests, using a different sample geometry, are required to determine whether shear experiments on disaggregated gouge provide a good proxy for intact sample resistivity.

5. Discussion

5.1. Sample Resistivity, Porosity, and Surface Conductivity

In Figure 7 we plot conductivity as a function of porosity for selected core samples. The foliated gouge that comprises the core of the active central deforming zone is the most conductive sample. Similar observations were found for the borehole logging data (Figure 3) where both SDZ and CDZ showed distinct drops in resistivity. Both of these zones are characterized by high concentrations of saponite, a Mg-rich smectite clay, that is apparently formed by metasomatic reactions between serpentinite, entrained in the fault zone, and adjoining sedimentary rocks [Lockner et al., 2011; Moore and Rymer, 2007, 2012]. Due to the high cation exchange capacity (CEC) of smectites, the high gouge conductivity may be the result of surface conduction in the clay. Alternatively, the foliated gouge sample had high porosity, and therefore high pore water content, which would also contribute to conductivity.

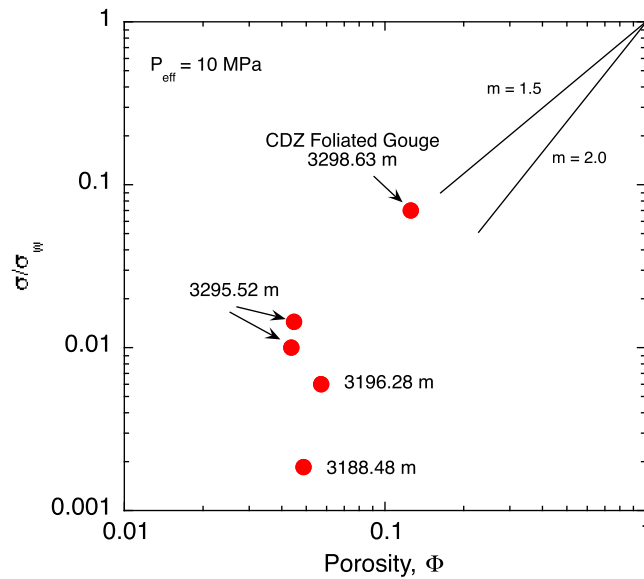


Figure 7. Normalized sample conductivity (σ/σ_w) as a function of porosity for selected samples at $P_{eff} = 10$ MPa. Average cementation factor is $m = 1.6$. The relative high conductivity of the foliated gouge is due to gouge porosity and surface conduction in the clay.

While equation (4) is useful for describing clean sandstone conductivity, a more complex formulation is required for shaly sands or fault gouge that contains clays and other phyllosilicates. In this case, charge defects within the mineral crystal structure attract ions dissolved in the pore fluid. The double layer that spontaneously forms on the mineral surfaces is composed of loosely bound water and solvated ions with

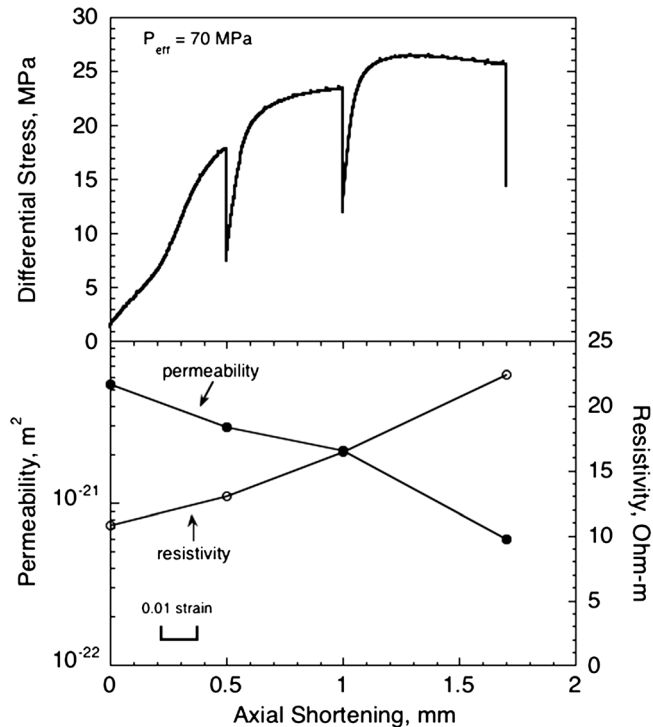


Figure 8. Axial shortening of an intact gouge sample (3298.63 m, CDZ) to 10% strain (1.7 mm). Resistivity and permeability were measured at 0, 0.5, 1.0, and 1.7 mm.

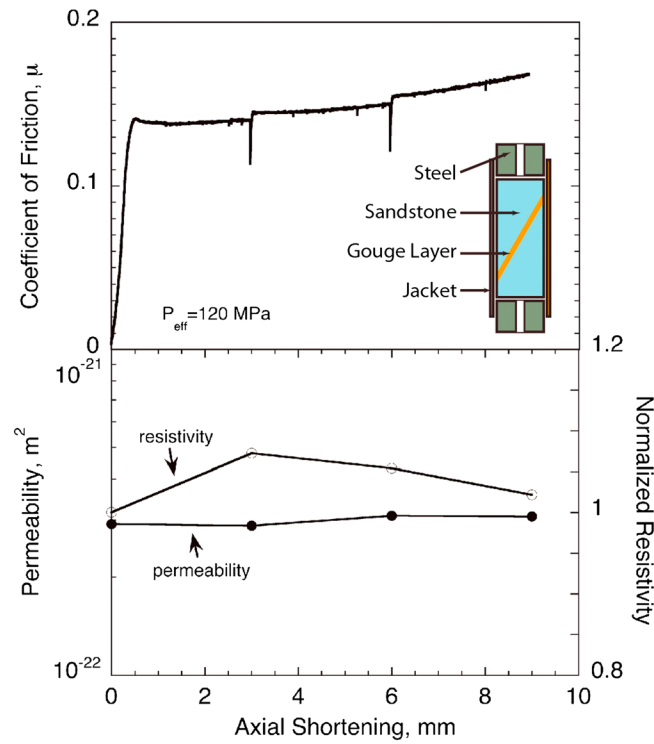


Figure 9. Permeability, electrical resistivity (normalized to the value at zero axial shortening), and the coefficient of friction for a disaggregated gouge from the CDZ (3296.86 m) during shearing. A 2 mm layer of gouge was sheared between 30° saw cut cylinders of Berea sandstone (inset shows the sample configuration). Permeability and resistivity showed little variation with shearing.

(dioctahedral) share similar structural forms. If we use $Q_v = 2320 \text{ meq L}^{-1}$ for montmorillonite and adjust for its weight fraction [Revil et al., 1998], we obtain a reasonable estimate of charge density for the foliated gouge of $Q_v \sim 1390 \text{ meq L}^{-1}$. (Similar values were reported by Waxman and Smits [1968] for “very shaly” samples.) Then, $\sigma_s = 6.39 \text{ S m}^{-1}$ and as measured separately, we have $\sigma_w = 3.4 \text{ S m}^{-1}$ and $\phi = 0.124$. The measured sample conductivity ($\sigma = 0.243 \text{ S m}^{-1}$) requires $m = 1.7 \pm 0.2$. The Waxman-Smits model predicts that by including surface conduction, the sample conductivity is about 2.5 times greater than if there were no surface conduction.

A key assumption of the Waxman-Smits model is that surface and bulk conduction use the same flow paths. This is inconsistent with the structure of the electrical double layer that contains the surface charge carriers [Bussian, 1983; Revil et al., 1998]. Using a generalized mixing law, Bussian [1983] developed an alternative expression for conductivity that assumes separate flow paths for surface and bulk conduction

$$\sigma = \sigma_w \phi^m \left(\frac{1 - \sigma_s / \sigma_w}{1 - \sigma_s / \sigma} \right)^m \quad (6)$$

To evaluate equation (6), undetermined parameters in our experiments are m and σ_s . For the foliated gouge, choosing a range of $m = 2.0 \pm 0.4$ requires $\sigma_s = 0.16 \pm 0.03 \text{ S m}^{-1}$. The Bussian model predicts that the foliated gouge is about 5.5 times more conductive than it would be if there were no surface conduction.

Finally, Revil et al. [1998] developed a dual water model incorporating the Bussian mixing law combined with estimates of specific ion mobilities within the Stern layer. Using their equation (10), conductivity is expressed as

$$\sigma = \sigma_w \phi^m \left[1 - t + \xi \phi^{-m} + \frac{t - \xi}{2} \left(1 - \frac{\xi}{t} + \left(\left(1 - \frac{\xi}{t} \right)^2 + \frac{4\xi}{t} \phi^{-m} \right)^{1/2} \right) \right] \quad (7)$$

where t is the fractional cation mobility ($t(\text{Na}^+) \sim 0.38$ in aqueous NaCl) and $\xi = \sigma_s / \sigma_w$ is the ratio of surface conductivity to bulk fluid conductivity [Revil et al., 1998]. For the foliated gouge, we find $\sigma_s = 0.18 \pm 0.05 \text{ S m}^{-1}$.

properties that differ from those in the bulk fluid. Ions in the Stern layer adjacent to the mineral surface are primarily responsible for the observed surface conductivity σ_s [Revil et al., 1998, and references therein]. In this case, σ_s and σ_w (bulk electrolytic conductivity) both contribute to the observed sample conductivity σ . Waxman and Smits [1968] proposed a widely used model to account for the combined contributions of surface and bulk conductivity in shaly sands:

$$\sigma = (\sigma_w + \sigma_s) \phi^m. \quad (5)$$

They further developed a representation for surface conduction as $\sigma_s = BQ_v$, where B is the equivalent cationic conductance and Q_v is the concentration of cations. To evaluate equation (5) for the foliated gouge sample, we note that for high-salinity NaCl solutions at 25°C [Waxman and Smits, 1968], $B \sim 4.6 \times 10^{-6} \text{ S m}^2 \text{ meq}^{-1}$. The SDZ gouge is composed of approximately 60% saponite—a Mg-rich smectite clay. We do not have Q_v data for saponite. However, we note that saponite (trioctahedral) and montmorillonite

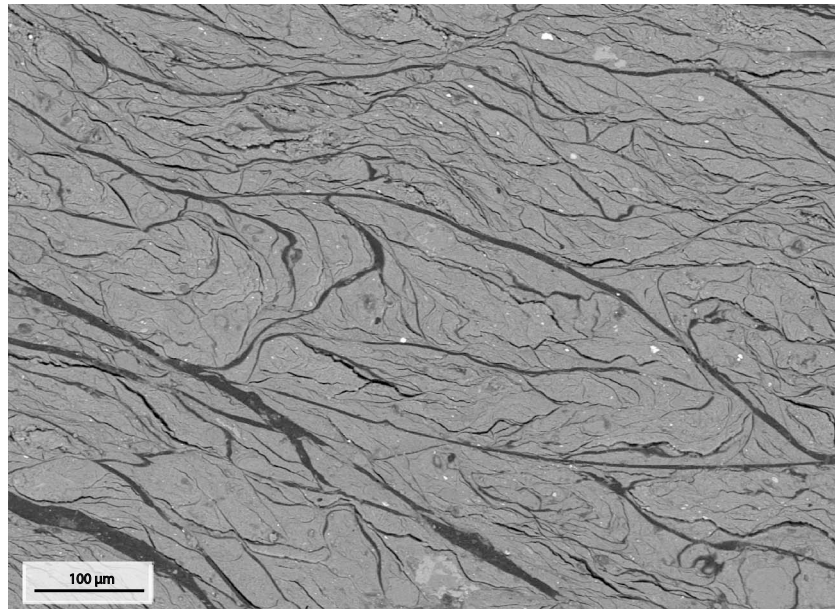


Figure 10. SEM image of a CDZ foliated gouge thin section from 3298.63 m. Anastomosing black lines (epoxy) indicate areas of porosity. Image by D. Moore.

The Revil et al. model uses the same basic mixing law as the Bussian model and also predicts that when surface conduction is included, the foliated gouge sample has approximately 5.5 times higher conductivity than it would without surface conduction. Thus, all three clayey-sand models suggest that surface and bulk electrolyte conduction are both important in contributing to the total foliated gouge conductivity and that surface conduction in the clays may dominate. Additional tests using different electrolyte concentrations would define the relative contributions of surface and bulk conductivity more clearly.

The remaining data plotted in Figure 7 are for samples outside of the actively deforming zones. X-ray diffraction (XRD) analysis of these samples indicates little or no saponite and varying amounts of other phyllosilicates. Samples 3188.48 and 3295.52 are predominantly quartz with minor feldspar, calcite, and phyllosilicates. Sample 3196.28 is wall rock bounding the SDZ and shows quartz + feldspar + calcite as well as appreciable Mg-clays. All of these samples have porosity of 4–6% and show evidence for healing and sealing of existing fractures [Holdsworth et al., 2011]. By contrast, the CDZ foliated gouge sample has 12.4% porosity which, as seen in Figure 7, can account for much of its higher conductivity. There is clear evidence for precipitation and recrystallization within the foliated gouge when viewed in thin section [Moore, 2014]. Since these processes should destroy porosity, the observed large porosity of the foliated gouge, even at high confining pressure, may be the result of active deformation [Barton et al., 1995]. The anastomosing microstructure of the foliated gouge, as well as the tendency for open porosity, can be seen in the scanning electron microscope (SEM) image shown in Figure 10.

Surface conduction is likely to play a minor role for many of the samples outside of the foliated gouge zone since clay content, especially high CEC smectite clay, is often low. For example, if we apply equation (5) to sample 3188.48 and assume a phyllosilicate content of <10%, as suggested by XRD data, we obtain $Q_v < 232 \text{ meq L}^{-1}$. This is probably an overestimate of Q_v since the phyllosilicates present in this sample may have much lower CEC than the montmorillonite value assumed here. Then, equation (5) predicts $\sigma_s < 1.1 \text{ S m}^{-1}$ and surface conduction contributes less than a quarter of the total conductivity. A similar analysis, using equation (7), also predicts that surface conduction in sample 3188.48 is minor.

Additional tests are required to more precisely identify the factors controlling gouge resistivity. For example, measuring resistivity at progressively lower brine concentrations would result in a shift from bulk ionic conduction in the fluid to surface conduction on the clay particles and would allow a more accurate measure of the relative contribution of these current paths. Alternatively, clays are known to have reduced resistivity at

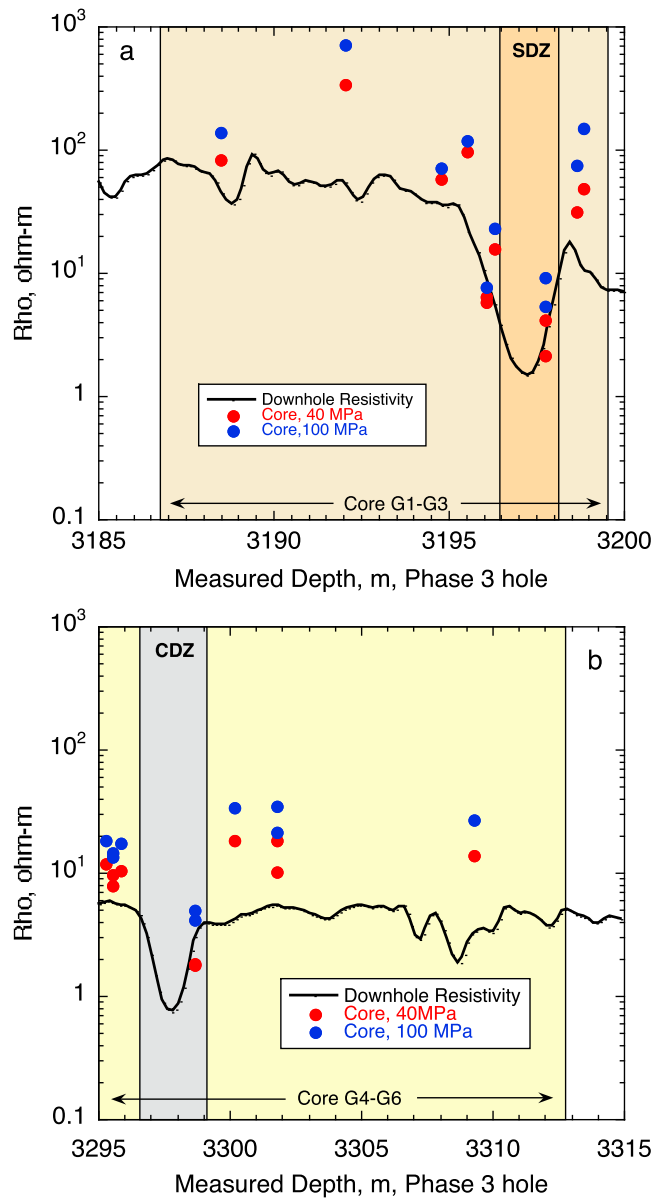


Figure 11. (a) Electrical resistivity as a function of depth for SAFOD samples from cores G1–G3, including the southwest deforming zone (SDZ). Values have been adjusted for brine conductivity at the in situ temperature of 113°C. Since pore pressure is not well constrained in the borehole, values at both 40 and 100 MPa effective pressure are plotted to show a possible range of in situ values. Resistivity from the Phase 2 downhole log (black line) has been depth shifted to match the depth of the SDZ in Phase 3. (b) Similar plot for cores G4–G6, including the central deforming zone (CDZ), and downhole resistivity (black line).

low frequency including a $(\text{frequency})^{-1/2}$ dependence (Warburg impedance) that is indicative of a diffusion transport mechanism. This surface conduction mechanism typically becomes important below about 100 Hz. Neither of these types of tests has yet been conducted on the SAFOD samples.

5.2. Comparison of Downhole and Laboratory Resistivity

The laboratory-derived resistivity values in and around the two deforming zones are shown in Figure 11 along with downhole resistivity log data (120"/3.05 m DOI) that have been depth shifted to account for the difference between Phases 2 and 3 measured depths. The downhole data represent resistivity averaged over about a 1.5 m interval due to the resolution of the probe. Thus, sharp resistivity contrasts at the boundaries of the SDZ and CDZ are blurred to some degree, and the minima in the downhole log represent upper bounds

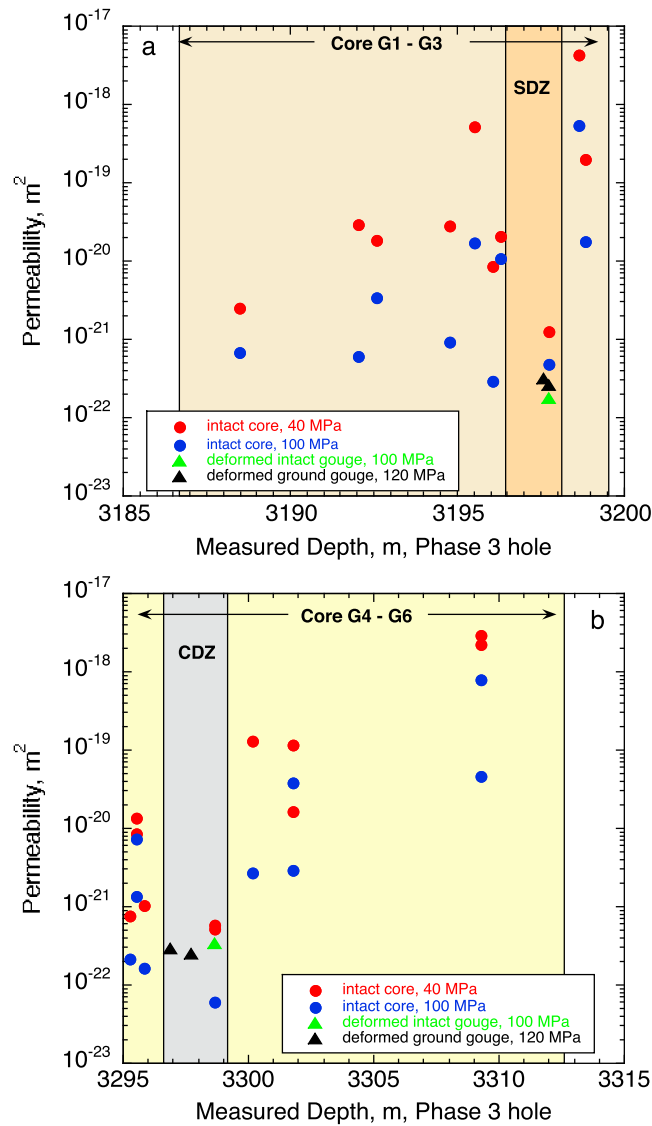


Figure 12. (a) Permeability as a function of depth for SAFOD samples from cores G1–G3, including the southwest deforming zone (SDZ). Data at both 40 and 100 MPa are included to show a possible range of in situ values. (b) Permeability of cores G4–G6 including the central deforming zone (CDZ).

of the deforming zone resistivity. Velocity and natural gamma logs (Figure 3) have similar resolution. Temperature logs carried out after Phase 2 drilling showed a temperature gradient of $\sim 0.02^\circ\text{C}/\text{m}$ in the inclined portion of the SAFOD borehole. The temperature is 112°C at the SDZ which marks the SW boundary of the roughly 200 m wide damage zone. CDZ temperature near the center of the damage zone is 114°C . Laboratory resistivity data, measured at 23°C , must be adjusted for comparison to in situ resistivity log data at this elevated temperature. A 90°C temperature difference would reduce bulk water resistivity by a factor of 3.8 [Hayashi, 2004]. Mobility of adsorbed surface ions has a different temperature dependence and would be expected to decrease resistivity by a factor of 4.6 [Revil et al., 1998]. Thus, the relative contributions of surface and bulk conductivity become important in adjusting the room temperature laboratory measurements to in situ conditions. As shown in section 5.1, surface conduction probably plays a minor role in conductivity of most of the samples tested. However, samples were specifically selected to avoid macroscopic fractures that might contain greater abundance of phyllosilicates with enhanced surface conductivity. We will use the correction factor of 3.8 and recognize that it will provide an upper bound on resistivity under in situ conditions. Consequently, laboratory resistivity values plotted in Figure 11 have been reduced by this factor relative to the values shown in

Figures 5a and 5b. In addition, because resistivity of the core samples varies with pressure and the in situ effective pressure in the SAFOD borehole is not well constrained, we plot resistivity for each core sample at both 40 and 100 MPa to show a range of possible in situ values. Both downhole and laboratory data show as much as an order of magnitude decrease in resistivity in the deforming zones compared to the damage zone/country rocks on either side. There is also more variability in resistivities of rock surrounding the SDZ (7 to 700 Ω -m) compared to the CDZ (8 to 30 Ω -m), although this could reflect the limited number of samples that we tested. Laboratory-determined resistivities are systematically higher than the corresponding borehole log resistivities by a factor of 2 to 3. Similar scaling issues were observed when comparing laboratory and downhole seismic velocity [Jeppson and Tobin, 2013, 2015]. They found that laboratory-derived P wave velocities in the damage zone were higher than the sonic log measurements and attributed this to larger-scale features such as fractures and small faults that were picked up in the sonic log, reducing the average velocity.

We were careful to select core samples for the combined resistivity/permeability measurements that avoided open fractures and would provide physical properties of the rock matrix. Consequently, as with the velocity measurements, we would expect our resistivity measurements to be systematically higher (and permeability measurements to be lower) than in situ measurements that include contributions from both matrix and fractures. It is also possible that the test brine we used (0.38 mol/L) had lower salinity than the in situ formation fluid within the fault damage zone. A factor of 2 difference in resistivity could be achieved by increasing test fluid molarity to about 0.7 mol_{NaCl}/L. This is a brine concentration slightly higher than seawater. Furthermore, we have not accounted for the possible effects of preferred fracture orientation in the damage zone and country rock, that may result in resistivity (and permeability) anisotropy, as all samples were oriented parallel to the axis of the borehole.

5.3. Permeability

The general form of the resistivity plot as a function of depth in Figure 11 is echoed in the corresponding permeability plot (Figure 12). Here we also show 40 and 100 MPa effective pressure data to reflect the range of possible in situ values. Data for selected deformed samples at specific pressures are also included. Permeability values of the entire suite of core samples covered 5 orders of magnitude, partly reflecting rock type, but also the fact that a few of the damage zone and country rock samples contained visible fractures, which greatly enhanced fluid flow. In fact, the presence or absence of fractures is what generally makes permeability data scale dependent [Brace, 1984], although in this case we have no in situ measurements for comparison with our centimeter-scale laboratory samples. Permeability was lower in the SDZ and CDZ compared to the surrounding damage zone rocks, ranging between 10^{-21} and 10^{-22} m², due to the high clay content (60–65%) of these samples. Unlike the formation factor shown in Figure 7, there is no simple empirical relation between permeability and porosity. Therefore, the higher porosity of the foliated gouge samples does not translate into higher permeability. A number of theoretical equations have been derived to describe permeability that build on the principles of flow through capillary tubes, such as the well-known Kozeny-Carman equation [Mitchell, 1993],

$$k = \frac{1}{k_0 T^2 S^2} \frac{e^3}{(1 + e)} \quad (8)$$

where k_0 is a pore shape factor, T is a tortuosity factor, S is the specific surface of the solids (a measure of pore size), and e is the void ratio ($e = \phi/(1 - \phi)$). Thus, k should vary with $e^3/(1 + e)$. Equation (8) accounts well for the dependence of permeability on void ratio in cohesionless sands but is less successful for clay-rich material because clays do not contain uniform pore sizes and also tend to exhibit a strong fabric. (See Moore and Rymer [2012] and Moore [2014] for a complete discussion of fabric and textures in the SAFOD gouge and damage zone material). All of these factors lead to our observation that the clay-rich samples have a lower permeability than the surrounding rocks in spite of having the highest porosity.

The extremely low permeability values (between 10^{-21} and 10^{-22} m²) in the deforming zones shown in Figure 12 imply that these zones will act as a cross-fault barrier to fluid flow [Morrow et al., 2014]. This is supported by mud gas analyses carried out across the San Andreas Fault at SAFOD [Wiersberg and Erzinger, 2008, 2011].

5.4. Strength of Clay Gouge

Figures 8 and 9 showed that differential stress and the coefficient of friction of sheared foliated gouge ($\mu < 0.2$) fell well below values typically associated with Byerlee's law ($\mu \sim 0.6$) [Byerlee, 1978]. These two

CDZ samples contain a large percentage of the Mg-rich phyllosilicate mineral saponite, the implications of whose low strength is discussed elsewhere [Lockner *et al.*, 2011; Carpenter *et al.*, 2012]. Adsorbed water is known to significantly lower shear strength of many phyllosilicates [Morrow *et al.*, 2000; Moore and Lockner, 2007]. However, our interest in the deformation tests (Figures 8 and 9) is in how resistivity and permeability responded during shortening and shearing of the CDZ gouges rather than in the specific strength of the material. As expected, we found that during deformation and shearing, permeability and resistivity values varied inversely, just as they did when effective pressure was increased (Figure 6). Resistivity of the foliated gouge at zero strain (Figure 8) matched the hydrostatic value at 70 MPa ($\sim 10 \Omega\text{-m}$) shown in Figure 5b. After 10% strain, resistivity had increased to around $22 \Omega\text{-m}$ due to compaction of the sample under an axial load. While effective confining pressure was held constant during the deformation test shown in Figure 8, effective mean stress $((\sigma_1 + \sigma_3)/2 - P_p)$ increased to 83 MPa at 10% strain. If resistivity varies to first order with mean stress, then the expected resistivity (taken from $P_{\text{eff}} = 83 \text{ MPa}$ in Figure 5b) would be $\sim 14 \Omega\text{-m}$. The observed increase in resistivity at 10% strain was 3 times this, suggesting that shearing has a significant effect on resistivity of the gouge material.

We have only measured resistivity in the axial direction (σ_1). Since compression in the axial direction can cause cracks to open up in other orientations depending on the fabric and fracture orientation of the material, the resulting resistivity parallel to σ_2 or σ_3 may be neutral or decreased. In fact, this same principal applies to damage zone and country rock samples as well. That is, preferred orientation of fractures will produce anisotropy in both resistivity and permeability. Measuring anisotropy, however, is beyond the scope of the present study. The mean stress calculation presented above does not work well for estimating the concurrent permeability decrease during 10% axial strain shown in Figure 8. Permeability decreased by an order of magnitude, whereas using the pressure sensitivity shown in Figure 5d predicts a decrease in permeability of only a factor of 2. Apparently, shearing is significantly more efficient at altering pore geometry and therefore both resistivity and permeability than simple hydrostatic pressurization.

The steady change in permeability and resistivity during deformation of an intact sample (Figure 8) would seem inconsistent with the nearly constant permeability and resistivity during shearing of the 2 mm saw cut gouge layer experiment (Figure 9). However, it should be noted that the total strain achieved in the intact sample is roughly equivalent to the initial strain hardening that occurred in the saw cut geometry by 0.5 mm shortening. The final permeability attained in the intact sample following peak stress was equivalent to the permeability throughout the saw cut experiment. Apparently, the permeability measured perpendicular to the shearing direction in the saw cut geometry is sensitive to the initial placement of the gouge layer as described above.

It was found in Morrow *et al.* [2014] that disaggregated gouge could be used as a proxy for intact samples for permeability measurements during shearing because the intact and disaggregated samples gave similar results. This is advantageous when intact core samples are scarce or difficult to work with. We believe, based on the permeability and resistivity response seen in Figure 9, that disaggregated sheared samples could also provide a good proxy for the resistivity of intact samples at larger strains. However, a sample configuration that used conductive driving blocks would be needed to confirm this.

6. Conclusions

Laboratory measurements correlate well with the downhole log data, although values can be scale dependent, as was also observed with comparisons of laboratory-derived and downhole velocity measurements [Jeppson and Tobin, 2015] and permeability measurements compiled by Brace [1984]. Resistivity of the deforming zones (1 to $10 \Omega\text{-m}$) was an order of magnitude lower than the surrounding damage zone and country rocks, making resistivity logs a good tool for detecting fault zone conductors. This low resistivity is correlated with the presence of conductive clays that are common constituents of shallow active faults. In the present study, the low resistivity appears to be the result of both higher porosity in the clay (probably the result of active deformation) and enhanced conductivity due to surface conduction. Although the downhole measurements broadly correlate with resistivity models from Unsworth *et al.* [2000] and Unsworth and Bedrosian [2004], the small dimensions of our laboratory samples precludes a similar comparison with MT observations across the San Andreas Fault owing to the vastly different scales.

Permeability was inversely related to resistivity during both hydrostatic and deformation experiments. Permeability values for all of the samples ranged over 5 orders of magnitude ($\sim 10^{-17}$ to 10^{-22} m^2) under

simulated in situ pressure conditions but was consistently low in the deforming zone foliated gouge samples ($\sim 10^{-21}$ to 10^{-22} m²). The low permeability in the deforming zone samples implies little cross-fault fluid flow in the San Andreas Fault.

Appendix A: SAFOD Phase 2 and Phase 3 Measured Depths

The following description of the procedure for aligning measured depth of the Phase 2 wireline resistivity log data and measured depth of the Phase 3 core is reproduced from the supporting information to “Scientific Drilling Into the San Andreas Fault Zone” [Zoback *et al.*, 2010].

Since the Phase 3 SAFOD borehole was drilled as a multilateral branching off of the Phase 2 hole, synchronizing depths between the Phase 3 core and the Phase 2 geophysical logs that define the location, physical properties and deformational behavior of the San Andreas Fault Zone are more complex. Accordingly, a variety of techniques were employed to map the SDZ and CDZ as revealed in the Phase 2 open hole and PMIT logs into the Phase 3 core:

1. Using open hole natural gamma and resistivity logs acquired across the SDZ in both the Phase 2 and Phase 3 holes. Owing to hole stability problems, these logs could only be run in the Phase 3 hole across the SDZ, as access to the CDZ was blocked by hole collapse following coring.
2. Using open hole natural gamma logs acquired in the Phase 2 hole across both the SDZ and CDZ, in concert with high-resolution spectral gamma scans run in the laboratory on the entire Phase 3 core.
3. Using offsets in distinctive methane peaks identified near the CDZ during drilling of Phases 2 and 3 through real-time analysis of gasses dissolved in the drilling mud (T. Wiersberg, personal communication).

The first and second techniques take advantage of the fact that (1) both the SDZ and CDZ are associated with an anomalously low total natural gamma count in the open hole geophysical logs and (2) both intervals of foliated fault gouge in the Phase 3 core—the 1.6 m associated with the SDZ and the 2.6 m associated with the CDZ—have a distinctively low total natural gamma signature relative to the rest of the core. In this manner, for the SDZ, we determined that 5.03 m should be *subtracted* from the depths indicated for the Phase 3 core to synchronize it to the Phase 2 Baker-Atlas open hole logs collected on 11 August 2005 [Zoback *et al.*, 2010, Figures 2a and 2b]. In contrast, for the CDZ, 3.96 m should be *added* to the depths indicated for the Phase 3 core to synchronize its depths to the Phase 2 Baker-Atlas open hole logs. Once these depth shifts are applied, both the SDZ and CDZ show a clear juxtaposition of (1) the actively deforming zones identified in the repeat casing deformation (PMIT) logs, (2) the low *P* and *S* wave velocity zones identified in the Phase 2 open hole logs [Zoback *et al.*, 2010, Figure 2b], and (3) the foliated fault gouge recovered in the Phase 3 core.

Acknowledgments

Supporting data for this paper are included in Table 1. Additional data may be obtained from C.M. (e-mail: cmorrow@usgs.gov). This project was funded by NEHRP. Thanks to Malcolm Johnston, Stephen Park, Hiroki Sone, and an anonymous reviewer for their helpful comments and suggestions.

References

- Archie, G. E. (1942), Electrical resistivity log as an aid in determining some reservoir characteristics, *Trans. Am. Inst. Min. Eng.*, *146*, 54–61.
- Barton, C. A., M. D. Zoback, and D. Moos (1995), Fluid flow along potentially active faults in crystalline rock, *Geology*, *23*, 683–686.
- Brace, W. F. (1984), Permeability of crystalline rocks: New in situ measurements, *J. Geophys. Res.*, *89*(6), 4327–4330, doi:10.1029/JB089iB06p04327.
- Bradbury, K. K., J. P. Evans, J. S. Chester, F. M. Chester, and D. L. Kirschner (2011), Lithology and internal structure of the San Andreas Fault at depth based on characterization of Phase 3 whole-rock core in the San Andreas Fault Observatory at Depth (SAFOD) borehole, *Earth Planet. Sci. Lett.*, *310*, 131–144, doi:10.1016/j.epsl.2011.07.020.
- Bussian, A. E. (1983), Electrical conductance in a porous medium, *Geophysics*, *48*(9), 1258–1268.
- Byerlee, J. (1978), Friction of rocks, *Pure Appl. Geophys.*, *116*, 615–626.
- Carpenter, B. M., D. M. Saffer, and C. Marone (2012), Frictional properties and sliding stability of the San Andreas Fault from deep drill core, *Geology*, *40*(8), 759–762, doi:10.1130/G33007.1.
- Hayashi, M. (2004), Temperature-electrical conductivity relation of water for environmental monitoring and geophysical data inversion, *Environ. Monit. Assess.*, *96*, 119–128.
- Holdsworth, R. E., E. W. E. van Diggelen, C. J. Spiers, J. H. P. de Bresser, R. J. Walker, and L. Bowen (2011), Fault rocks from the SAFOD core samples: Implications for weakening at shallow depths along the San Andreas Fault, California, *J. Struct. Geol.*, *33*(2), 132–134, doi:10.1016/j.jsg.2010.11.010.
- Hung, J., Y. Wu, E. Yeh, and J. Wu (2007), Subsurface structure, physical properties, and fault zone characteristics in the scientific drillholes of Taiwan Chelungpu-fault drilling project, *Terr. Atmos. Ocean. Sci.*, *18*(2), 271–293.
- Jeppson, T., and H. Tobin (2013), Physical properties of fault zone rocks from SAFOD: Tying logging data to high-pressure measurements on drill core, *Eos Trans. AGU*, Fall meeting supplemental.
- Jeppson, T., and H. Tobin (2015), San Andreas Fault zone velocity structure at SAFOD at core, log and seismic scales, *J. Geophys. Res. Solid Earth*, *120*, 4983–4997, doi:10.1002/2015JB012043.
- Lockner, D. A., and J. D. Byerlee (1985), Complex resistivity of fault gouge and its significance for earthquake lights and induced polarization, *Geophys. Res. Lett.*, *12*, 211–214, doi:10.1029/GL012i004p00211.
- Lockner, D. A., and J. D. Byerlee (1986), Changes in complex resistivity during creep in granite, *Pure Appl. Geophys.*, *124*, 659–676.

- Lockner, D., C. Morrow, D. Moore, and S. Hickman (2011), Low strength of deep San Andreas Fault gouge from SAFOD core, *Nature*, *472*, 82–85, doi:10.1038/nature09927.
- Mazzella, A. (1976), Deep resistivity study across the San Andrea Fault zone, PhD thesis, Univ. of Calif., Berkeley.
- Mitchell, J. K. (1993), *Fundamentals of Soil Behavior*, 437 pp., John Wiley, New York.
- Moore, D. (2014), Comparative mineral chemistry and textures of SAFOD fault gouge and damage-zone rocks, *J. Struct. Geol.*, *68*, 82–96, doi:10.1016/j.jsg.2014.09.002.
- Moore, D., and D. Lockner (2007), Friction of the smectite clay montmorillonite: A review and interpretation of data, in *The Seismogenic Zone of Subduction Thrust Faults, Margins Theoretical and Experimental Earth Science Series*, vol. 2, edited by T. H. Dixon and C. Moore, pp. 317–345, Columbia Univ. Press, New York.
- Moore, D., and M. Rymer (2012), Correlation of clayey gouge in a surface exposure of serpentinite in the San Andreas Fault with gouge from the San Andreas Fault at Depth (SAFOD), *J. Struct. Geol.*, *38*, 51–60, doi:10.1016/j.jsg.2011.11.014.
- Moore, D. E., and M. J. Rymer (2007), Talc-bearing serpentinite, and the creeping section of the San Andreas Fault, *Nature*, *448*, 795–797.
- Morrow, C., D. Moore, and D. Lockner (2000), The effect of mineral bond strength and adsorbed water on fault gouge frictional strength, *Geophys. Res. Lett.*, *27*(6), 815–818, doi:10.1029/1999GL008401.
- Morrow, C., D. Lockner, D. Moore, and S. Hickman (2014), Deep permeability of the San Andreas Fault Observatory at Depth (SAFOD) core samples, *J. Struct. Geol.*, *64*, 99–114, doi:10.1016/j.jsg.2013.09.009.
- Olhoeft, G. R. (1980), Electrical properties of rocks, in *Physical Properties of Rocks and Minerals*, edited by Y. S. Touloukian, W. R. Judd, and R. F. Roy, chap. 9, McGraw-Hill, New York.
- Pezard, P., H. Ito, D. Hermitte, and A. Revil (2000), Electrical properties and alteration of granodiorites from the GSJ Hirabayashi hole, Japan, in *International Workshop of the Nojima Fault Core and Borehole Data Analysis, GSJ INTERim Rep. EQ/00/1 and USGS Open-File Rep. 000–129*, edited by H. Ito et al., pp. 255–262, Geol. Surv. of Japan, Tskuba, Japan.
- Phillips, W., and A. Kuckes (1983), Electrical conductivity structure of the San Andreas Fault in central California, *J. Geophys. Res.*, *88*(B9), 7467–7474, doi:10.1029/JB088iB09p07467.
- Revil, A., L. M. Cathles, S. Losh, and J. A. Nunn (1998), Electrical conductivity in shaly sands with geophysical applications, *J. Geophys. Res.*, *103*(B10), 23,925–23,936, doi:10.1029/98JB02125.
- Ritter, O., A. Hoffmann-Rothe, P. Bedrosian, U. Weckmann, and V. Haak (2005), Electrical conductivity images of active and fossil fault zones, in *High-Strain Zones: Structure and Physical Properties*, vol. 245, edited by D. Bruhn and L. Burlini, pp. 165–186, Geol. Soc. Spec. Publ., London.
- Timur, A., W. B. Hemphkins, and A. E. Worthington (1972), Porosity and pressure dependence of formation resistivity factor for sandstones, in *Trans. Can. Well Logging Soc. Fourth Formation Evaluation Symposium*, 18 pp.
- Unsworth, M., and P. Bedrosian (2004), Electrical resistivity structure at the SAFOD site from magnetotelluric exploration, *Geophys. Res. Lett.*, *31*, L12505, doi:10.1029/2003GL019405.
- Unsworth, M., P. Bedrosian, M. Eisel, G. Egbert, and W. Siripunvaraporn (2000), Along strike variations in the electrical structure of the San Andreas Fault at Parkfield, California, *Geophys. Res. Lett.*, *27*(18), 3021–3024, doi:10.1029/2000GL011476.
- Wannamaker, P., G. Jiracek, J. Stodt, T. Caldwell, V. Gonzales, J. McKnight, and A. Porter (2002), Fluid generation and pathways beneath an active compressional orogeny, The New Zealand Alps, inferred from magnetotelluric data, *J. Geophys. Res.*, *107*(B6), 2117, doi:10.1029/2001JB000186.
- Waxman, M. H., and L. J. M. Smits (1968), Electrical conductivities in oil-bearing shaly sands, *Soc. Pet. Eng. J.*, *8*, 107–122.
- Wiersberg, T., and J. Erzinger (2008), Origin and spatial distribution of gas at seismogenic depths of the San Andreas Fault from drill-mud gas analysis, *Appl. Geochem.*, *23*, 1675–1690, doi:10.1016/j.apgeochem.2008.01.012.
- Wiersberg, T., and J. Erzinger (2011), Chemical and isotope compositions of drilling mud gas from the San Andreas Fault Observatory at Depth (SAFOD) boreholes: Implications on gas migrations and the permeability structure of the San Andreas Fault, *Chem. Geol.*, *284*, 148–159, doi:10.1016/j.chemgeo.2011.02.016.
- Yamaguchi, S., T. Murakami, and H. Inokuchi (2001), Resistivity mapping using the VLF-MT method around surface fault ruptures on the 1995 Hyogo-ken Nabe earthquake, Japan, *Isl. Arc*, *10*, 296–305.
- Yamaguchi, S., H. Murakami, H. Iwamoto, K. Takemoto, K. Kitada, I. Shoizaki, N. Oshiman, and S. Katoh (2007), Two-dimensional resistivity structure of the fault associated with the 2000 Western Tottori earthquake, *Earth Planets Space*, *59*, 1211–1217.
- Yang, C.-H., P.-H. Cheng, J.-I. You, and L. Tsai (2002), Significant resistivity changes in the fault zone associated with the 1999 Chi-Chi earthquake, west-central Taiwan, *Tectonophysics*, *350*, 299–313.
- Zoback, M., S. Hickman, and W. Ellsworth (2010), Scientific drilling into the San Andreas Fault zone, *Eos Trans. AGU*, *91*(22), 197–204, doi:10.1029/2010EO220001.
- Zoback, M., S. Hickman, and W. Ellsworth (2011), Scientific drilling into the San Andreas Fault zone: An overview of SAFOD's first five years, *Sci. Drill.*, *11*, 14–28, doi:10.2204/iodp.sd.11.02.2011.